Chinese Chemical Letters 36 (2025) 109987

Contents lists available at ScienceDirect

Chinese Chemical Letters

journal homepage: www.elsevier.com/locate/cclet

Excellent structural stability and electrochemical properties of $LiNi_{0.9}Co_{0.05}Mn_{0.05}O_2$ material by surface Ni^{2+} anchoring and Cs^+ doping

Hongyu Tang[a], Dongming Liu[b], Jinfu Huang[a], Liang Zhang[a], Yang Tang[a], Bin Huang[a], Yanwei Li[a], Shunhua Xiao[a,*], Yiling Sun[b,*], Renheng Wang[b,c,*]

[a] Guangxi Colleges and Universities Key Laboratory of Surface and Interface Electrochemistry, Guangxi Key Laboratory of Electrochemical and Magneto-chemical Functional Materials, College of Chemistry and Bioengineering, Guilin University of Technology, Guilin 541004, China
[b] Key Laboratory of Optoelectronic Devices and Systems of Ministry of Education and Guangdong Province, State Key Laboratory of Radio Frequency Heterogeneous Integration (Shenzhen University), College of Physics and Optoelectronic Engineering, Shenzhen University, Shenzhen 518060, China
[c] Key Laboratory of Advanced Energy Materials Chemistry (Ministry of Education), Nankai University, Tianjin 300071, China

ARTICLE INFO

Article history:
Received 16 February 2024
Revised 15 April 2024
Accepted 9 May 2024
Available online 15 May 2024

Keywords:
$LiNi_{0.9}Co_{0.05}Mn_{0.05}O_2$ material
Cs^+ doping
PMMA coating
Electrochemical performance
Electrochemical mechanism

ABSTRACT

The ultra-high nickel cathode material has important application prospect in power lithium-ion batteries. However, the poor structural stability and serious surface/interfacial side reactions during long cycles severely hinder the material's practical application. In this paper, Cs^+ doping and polymethyl methacrylate (PMMA) coating are used to synergistically modify the NCM955 material. The results show that the corresponding discharge specific capacity of NCMCs-2@P-2 material reaches 152.02 mAh/g at 1 C (1 C = 200 mA/g) and 125.66 mAh/g at 5 C after 300 cycles, and the capacity retention is 78.11% and 72.21%, respectively. In addition, it still maintains 156.36 mAh/g discharge specific capacity at 10 C, and these rate and cycle properties exceed those reported on ultra-high nickel cathode material. Moreover, NCMCs-2@P-2 material has higher migration energy barrier of Ni^{2+} and lower migration energy barrier of Li^+ than that of NCM955 material. Therefore, NCMCs-2@P-2 material has excellent electrochemical properties, which has been proved by a series of structural characterization, theoretical calculation and performance test. The synergistic enhancement of Cs^+ doping and PMMA coating accelerates lithium ion diffusion kinetics, stabilizes crystal structure, and inhabits surface/interface side reaction.

Lithium-ion batteries (LIBs) have developed rapidly in recent decades, and are widely used in electric vehicles and energy storage devices because of their high reversible specific capacity and operating voltage [1–5]. $LiNi_xCo_yMn_zO_2$ (NCM, $x+y+z=1$) ternary material, which is similar to $LiCoO_2$ layer structure and has high specific capacity, is an important cathode material for power lithium-ion batteries and has broad application prospects [6–9].

In the process of charge and discharge of NCM material, when lithium ions are detached, Co^{3+} becomes Co^{4+}, and Ni^{2+}/Ni^{3+} becomes Ni^{4+} to maintain the stability of the structure, while the situation is exactly opposite when lithium ions are embedded [9]. However, the actual specific capacity is about 160 mAh/g, and some Ni^{2+} tends to migrate to the Li^+ position, resulting in structural changes [10]. The specific capacity of NCM material can be increased by increasing the Ni content, so the high-nickel material $LiNi_xCo_yMn_zO_2$ ($x \geq 0.8$) is highly concerned as a new type of power battery [11,12]. Moreover, as the Ni content increases and the Co content decreases, the cost of the material also decreases. However, with the increase of Ni content, the material structure becomes more unstable. On the one hand, the radius of Li^+ (0.076 nm) is similar to that of Ni^{2+} (0.069 nm), which can easily lead to Li/Ni mixing and the obstacle of Li^+ insertion/extraction, thereby reducing Li^+ diffusion rate [13,14]. On the other hand, when Li^+ is removed, the crystal structure changes irreversibly from the H2 phase to the H3 phase, resulting in the anisotropic contraction of the lattice, the formation of microcracks and even crystal collapse, and the aggravating side reaction with HF [15,16]. In addition, at the end of the charging process, the generated Ni^{4+} will trigger the release of oxygen and a series of side reactions with the electrolyte, resulting in material abnormalities and safety hazards [17].

* Corresponding authors.
E-mail addresses: 1999014@glut.edu.cn (S. Xiao), sunyl@szu.edu.cn (Y. Sun), wangrh@szu.edu.cn (R. Wang).

https://doi.org/10.1016/j.cclet.2024.109987
1001-8417/

At present, the modification methods mainly include ion doping and surface coating. Common ion doping includes cationic doping (Na [18], Mg [19], Al [20], Ti [21] and Mo [22], *etc.*) and anionic doping (F [23] and Cl [24], *etc.*), which can make the crystal structure of the material more stable. Common coatings include metal oxides (TiO_2 [25], Al_2O_3 [26] and V_2O_5 [27], *etc.*), lithium salt ($Li_2Si_2O_5$ [28], Li_2SO_4 [29] and Li_3PO_4 [30], *etc.*), metal fluoride (YF_3 [31], *etc.*) and organic coating (PANI [32], PDMS [33] and PMMA [34], *etc.*), which are considered to be an excellent coating for inhibiting surface/interface reactions.

Based on the above literature research, in this paper, a cooperative modification strategy is used to stabilize the crystal structure and interfacial chemical stability, *i.e.*, Cs^+ doped and PMMA coated NCM955 material was synthesized by high temperature solid phase method. The radius of Cs^+ (0.167 nm) is larger than that of Li^+ (0.076 nm), and its incorporation into the lattice expands the layer spacing, which can reduce the mixing of Li/Ni and increase the diffusion rate of Li^+. The ester group in the PMMA coating on the surface of the NCM955 material has an electron-absorbing feature, which helps to attract electrons from Ni^{2+} at the electrode interface. Moreover, the cyclic nickel-ester compound formed through the interatomic interaction can further anchor the surface Ni^{2+} and effectively inhibit the surface/interface side reaction [34]. A series of structural characterization proved that the synergistic strategies of Cs^+ doping and PMMA coating effectively reduce Li/Ni mixing, widen layer spacing, improve Li^+ diffusion rate and inhibit surface/interface side reactions. Electrochemical tests show that NCMCs-2@P-2 material has much better long cycle stability and rate performance than that of the pristine NCM955 material.

The precursor $Ni_{0.9}Co_{0.05}Mn_{0.05}(OH)_2$, $LiOH{\cdot}H_2O$ and $CsC_2H_3O_2$ were mixed and ground evenly according to the molar ratio of 1:1.05:x ($x = 0.015$, 0.02, 0.025). In a pure oxygen atmosphere, the first stage was roasted at 500 °C for 4 h, then at 750 °C for 11 h, and finally cooled to room temperature. The pristine $LiNi_{0.9}Co_{0.05}Mn_{0.05}O_2$ material was labeled as NCM955, while the materials with different Cs doping amounts were labeled as NCMCs-1, NCMCs-2 and NCMCs-3, respectively.

Added an appropriate amount of PMMA to the acetone and stirred in a water bath at 80 °C until the PMMA was completely dissolved, then added a certain amount of NCMCs-2 to PMMA solution (the mass ratio of NCMCs-2 to PMMA was NCMCs-2:PMMA = 1:(0.005, 0.01, 0.015) and stirred continuously for 2 h. The reactants were further filtered and dried in an oven at 110 °C for 24 h. The compounds with different PMMA coating amounts were labeled as NCMCs-2@P-1, NCMCs-2@P-2 and NCMCs-2@P-3, respectively. The corresponding schematic diagram of synthesis process was shown in Fig. 1a.

The crystal structure was characterized by X-ray diffractometer (XRD, X 'Pert PRO MRD, PANalytical, Netherlands) and Rietveld refinement of XRD data was performed by structural analysis software (GSAS II). The surface morphologies of as-synthesized materials were photographed by scanning electron microscopy (SEM, JSM-5612LV, JEOL, Japan), and the surface compositions of as-synthesized materials were measured by X-ray energy dispersive spectrometer (EDS, Quantax400, BRUKER, Germany). The microstructure of as-synthesized materials was characterized by transmission electron microscopy (TEM, FEI Tecnai F20, Fhermo Fisher Scientific, America). The surface elements were characterized by X-ray photoelectron spectrometer (XPS, K-Alpha, Thermo Fisher Scientific, America), and the corresponding XPS data were analyzed with XPSPEAK software. Qualitative analysis of PMMA was performed using Fourier transform infrared spectrometer (FTIR, Nicolet iS 10, Thermo Fisher Scientific, America).The cross-sectional morpology of the active material after cycling was studied by FIB-SEM (JSM-7800F, JEOL, Japan). Inductively coupled plasma (ICP-MS, NexION 300X, PerkinElmer, America) was used to determine the content of metal ions in the electrolyte after cycling.

The mechanism of Cs ion modification was deeply analyzed by density functional theory (DFT) based on first-principles calcula-

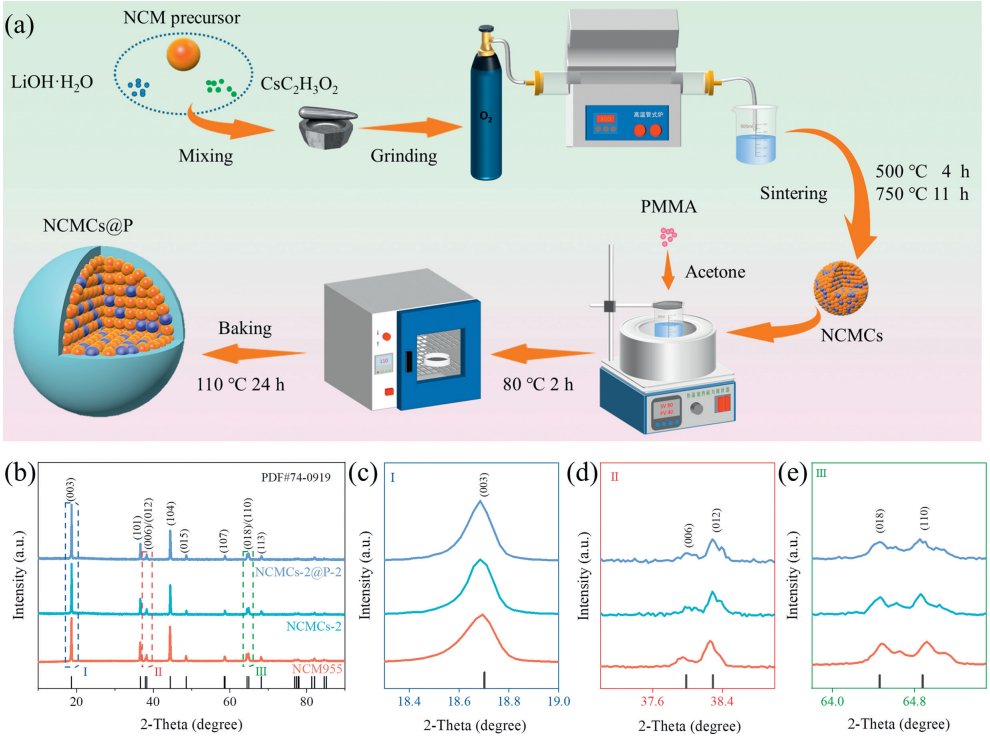

Fig. 1. (a) Schematic diagram of synthesis process of NCMCs@P. (b) XRD patterns of NCM955, NCMCs-2 and NCMCs-2@P-2. (c) Amplification of (003) peak. (d) Amplification of (006)/(012) peaks. (e) Amplification of (018)/(110) peaks.

Table 1
The lattice parameters of NCM955, NCMCs-2 and NCMCs-2@P-2 materials from Rietveld refinements.

Samples	a (Å)	c (Å)	V (Å^3)	c/a	I_{003}/I_{104}	Li/Ni mixing (%)	R_{wp} (%)	R_p (%)
NCM955	2.86956	14.17792	101.105	4.94080	1.220	3.53	4.226	2.856
NCMCs-2	2.86972	14.18087	101.138	4.94155	1.637	2.98	6.103	4.725
NCMCs-2@P-2	2.86967	14.18220	101.242	4.94160	1.789	2.79	6.064	4.660

tion. Theoretical calculation was carried out using Vienna *Ab-initio* Simulation Package (VASP) software. In the calculation process, Generalised Gradient Approximation (GGA)-Perdew Burke Ernzerho (PBE) was applied to the exchange-correlation function, and all plane-wave cutoff energy was 450 eV. For structural optimization, a $2 \times 2 \times 1$ Gamma center K-point grid was used in the Brillouin region, combined with DFT-D3 correction. In addition, the diffusion behavior and migration energy barrier of Li^+ and Ni^{2+} were analyzed using the Climbing Image Nudged Elastic Band (CI-NEB) method.

Firstly, active substance, carbon black and polyvinylidene fluoride (PVDF) were mixed evenly (the corresponding mass ratio was active substance:carbon black:PVDF = 8:1:1), and an appropriate amount of *N*-methyl-2-pyrrolidone (NMP) was added to make a fluid electrode slurry using a magnetic stirrer. Then, the slurry was evenly coated on the rough surface of the aluminum foil, and dried at 110 °C for 15 h, and the dried electrode plate was cut into wafer using cutting machine with an inner diameter of 12 mm. Finally, the CR-2025 button half battery was assembled in a glovebox filled with argon gas. Among them, the cut electrode wafer was used as the cathode, lithium plate as the negative electrode, porous polypropylene (Celgard 2400) as the diaphragm, and $LiPF_6$ containing vinyl carbonate, methyl ethyl carbonate and dimethyl carbonate (corresponding molar ratio was 1:1:1) as the electrolyte.

The assembled half battery was left at room temperature for 24 h, then the battery test system (BTS-4000, Shenzhen Newwell Co., Ltd., China) was used to test its electrochemical performances. At 25 °C and voltage window of 2.8–4.3 V, the half battery was cycled for 5 cycles at different current densities (0.2, 0.5, 1, 2, 3, 5 and 10 C, 1 C = 200 mA/g) to study the rate performance. Under the same voltage window, the half battery was charged and discharged for 300 cycles at 1 C and 5 C to analyze the cycle stability of the material.

The electrochemical workstation (CHI760e, Shanghai Chenhua Co., Ltd., China) was used to test the initial cyclic voltammetry (CV) curves at 2.8–4.3 V and 1 C, and the electrochemical impedance spectroscopy (EIS) curves at frequency of 10^{-2}–10^5 Hz and amplitude of 5 mV, respectively. The galvanostatic intermittent titration technique (GITT) and electrochemical impedance (EIS) data were used to calculate the Li^+ diffusion coefficient.

To understand the crystal structure of the material, XRD tests are carried out on NCM955, NCMCs-2 and NCMCs-2@P-2 materials. Fig. 1b is the total XRD spectra of the three materials. Figs. 1c–e are the (003) characteristic peak, the (006)/(012) split peak and the (018)/(110) split peak respectively, and Figs. S1a-c (Supporting information) are the corresponding Rietveld refinements of the three materials. Fig. 1b shows that the diffraction peaks of three materials are very sharp, indicating a good crystal structure [32,35]. All diffraction peaks correspond exactly to the standard card (PDF #74-0919) of hexagonal $LiNiO_2$, belonging to the α-$NaFeO_2$ layered structure of the *R*-3m space group and free of other impurity phases. This shows that Cs^+ doping and PMMA coating do not change the structure of the pristine material. In addition, the diffraction peaks of (006)/(012) and (018)/(110) are found to be obviously split, indicating that the three materials have a typical layered structure [36,37]. The XRD data are subjected to Rietveld refinement using GSAS II and the corresponding refinement results are shown in Table 1. Firstly, the reliability factor R_{wp} is less than 10%, which indicates the reliability and accuracy of the refinement [38,39]. Secondly, the (003)/(104) peak ratios reflect the degree of Li/Ni mixing [40–43]. The peak ratios of NCM955, NCMCs-2 and NCMCs-2@P-2 materials are 1.220, 1.637 and 1.789, respectively, which implies that the degree of Li/Ni mixing is effectively reduced with the Cs^+ doping and PMMA coating. Thirdly, Table 1 also reveals that the c/a values of NCM955, NCMCs-2 and NCMCs-2@P-2 materials gradually increase, indicating that the interlayer structure of the NCM955 material modified by Cs^+ and PMMA is more ordered [44–46]. Furthermore, the c values of the Cs^+ doped and PMMA coated materials are larger than that of pristine NCM955 material, it is manifested that the doped Cs^+ and coated PMMA can widen the interlayer spacing to some extent, which will be beneficial for accelerating the insertion/extraction efficiency of Li^+, and thus promoting the diffusion rate of Li^+.

Figs. 2a and b and Fig. S2 (Supporting information) show the SEM images of NCM955, NCMCs-2@P-2 and NCMCs-2 materials, respectively. It can be seen that a small amount of Cs doping has little effect on the size and morphology of the primary and secondary particles of NCM955 material, and the PMMA coating only smoothens the surface of the secondary particles but has little effect on the primary particles. Figs. 2d-i are the EDS images of NCMCs-2@P-2 material, and it can be found that the material simultaneously contains Ni, Co, Mn, O and doped Cs elements with a uniform distribution. The NCMCs-2@P-2 material is tested by TEM and the lattice fringe pattern is obtained using fast Fourier transform (FFT) and inverse fast Fourier transform (IFFT), as shown in Fig. 2c. It can be seen that there are obvious layered lattice fringes, and the lattice fringe spacing of the surface region is 0.239 nm, and the inner region is 0.237 nm, which are in accordance with the crystal plane (006) of the hexagonal $LiNiO_2$ standard card (PDF #74-0919) [47]. Obviously, the doping of Cs^+ effectively expands the lattice spacing, and the diffusion trend of Cs^+ gradually weakens from the outside to the inside. In addition, the presence of a thin coating is clearly seen on the surface of the NCMCs-2@P-2 material, which is tightly bonded to the material, and this should be the PMMA coating.

Fig. S3a (Supporting information) shows the full spectrum of XPS, and the characteristic peaks of Ni 2p, Co 2p, Mn 2p and O 1s can be found in all three materials. In particular, the Cs 3d characteristic peak, as well as the C–O and C=O characteristic peaks of PMMA are observed in NCMCs-2@P-2 material. Figs. 2j-o show the XPS spectra, which can quantitatively evaluate the surface element composition of NCM955 and NCMCs-2@P-2 materials.

Figs. 2j and k are the Ni 2p fine XPS spectra of NCM955 and NCMCs-2@P-2 materials, respectively. It can be found that Ni 2p splits into Ni $2p_{3/2}$ and Ni $2p_{1/2}$ peaks at 855.7 and 873.1 eV respectively, and the 854.8 and 856 eV split peaks at Ni $2p_{3/2}$ correspond to Ni^{2+} and Ni^{3+}, respectively [44,48]. By comparing the integral area of the splitting peak at Ni $2p_{3/2}$, it can be found that the Ni^{2+} content of NCMCs-2@P-2 material is 18.1%, which is lower than the 45.2% Ni^{2+} content of the pristine NCM955 material. It is proved that the Cs^+ doping and PMMA coating can effectively reduce the Li/Ni mixing, and further effectively stabilize the interlayer structure of the material [49,50]. Fig. S3d (Supporting information) and Fig. 2l are the Cs 3d characteristic peaks of

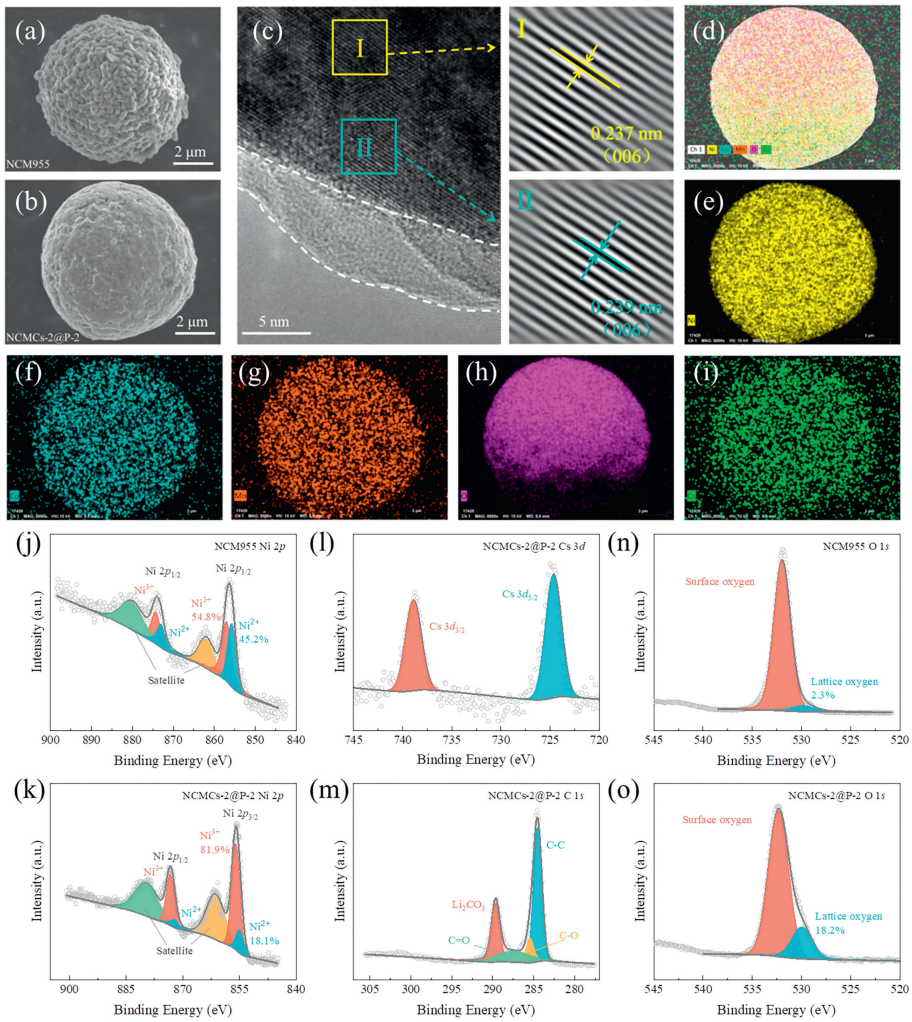

Fig. 2. SEM images of (a) NCM955 and, (b) NCMCs-2@P-2 materials. (c) TEM image of NCMCs-2@P-2 material and its corresponding fast Fourier transform (FFT) pattern. (d-i) EDS elemental mappings of Ni, Co, Mn, O and Cs for NCMCs-2@P-2 material. (j, k) Ni 2p fine spectra of NCM955 and NCMCs-2@P-2. (l) Cs 3d fine spectrum of NCMCs-2@P-2. (m) C 1s fine spectrum of NCMCs-2@P-2. (n, o) O 1s fine spectra of NCM955 and NCMCs-2@P-2.

NCMCs-2 and NCMCs-2@P-2 materials, respectively. It can be easily found that the two peaks of 724.8 and 740.0 eV correspond to Cs $3d_{5/2}$ and Cs $3d_{3/2}$, respectively, which is a valid evidence that Cs^+ is doped into the lattice of the material. Fig. 2m is the C 1s fine spectrum of the NCMCs-2@P-2 material, and the binding energies of 285.0, 285.4, 278.8 and 288.4 eV correspond to the characteristic peaks of C–C, C–O, C=O and Li_2CO_3 [34], respectively. However, there are no characteristic peaks of C=O and C–O appear in the C 1s fine spectra of NCM955 material in Fig. S3b (Supporting information) [34]. Furthermore, combined with the FTIR spectrum of Fig. S4 (Supporting information), the characteristic peaks of PMMA appear in NCMCs-2@P-2 material, which proves that PMMA is successfully coated on NCM955 material. Figs. 2n and o and Fig. S3c (Supporting information) are the O 1s fine XPS spectra of NCM955, NCMCs-2@P-2 and NCMCs-2 materials, respectively. It can be found that the characteristic peaks at 529.4 and 531.6 eV are the lattice oxygen (M-O) peak and surface adsorbed oxygen (LiOH and Li_2CO_3) of the material, respectively [45]. By comparing the lattice oxygen area and surface adsorbed oxygen area of the three materials, NCMCs-2@P-2 material has the largest lattice oxygen area and the smallest surface adsorbed oxygen area, indicating that PMMA coating effectively inhibits the side reaction between the material surface and H_2O and CO_2 in the air, and effectively eliminates the residual alkali on the surface of the material [1].

In order to investigate the electrochemical properties of the modified materials, charge-discharge tests are carried out between 2.8–4.3 V at 25 °C. The cycling performances of the materials with different doping and coating amounts are shown in Fig. S5 (Supporting information), which shows that the optimal doping amount is 2 at% (NCMCs-2, Fig. S5a) and the optimal coating amount is 1 wt% (NCMCs-2@P-2, Fig. S5b). Fig. 3a shows the initial charge-discharge curves of NCM955, NCMCs-2 and NCMCs-2@P-2 materials under 1 C at 25 °C. It can be seen that the corresponding discharge specific capacities are 192.98, 193.78 and 194.61 mAh/g, respectively. Fig. 3b shows the first cycle coulomb efficiency corresponding to Fig. 3a, and the first cycle coulomb efficiencies of NCM955, NCMCs-2 and NCMCs-2@P-2 materials are 78.24%, 81.18% and 82.98%, respectively, which indicates that Cs^+ doping and PMMA coating have no significant effect on the initial specific discharge capacity and coulomb efficiency. Fig. 3c shows the cycling performances of NCM955, NCMCs-2 and NCMCs-2@P-2 materials within the potential range of 2.8–4.3 V under 1 C at 25 °C. After 300 cycles, the discharge specific capacities of the three materials are 118.11, 146.67 and 152.02 mAh/g, respectively. The corresponding capacity retentions are 61.30%, 75.70% and 78.11%, respectively. Among them, NCM955 material has the worst capacity retention, followed by NCMCs-2 material, and NCMCs-2@P-2 material has the highest capacity retention. Comparatively, NCMCs-2@P-2 material

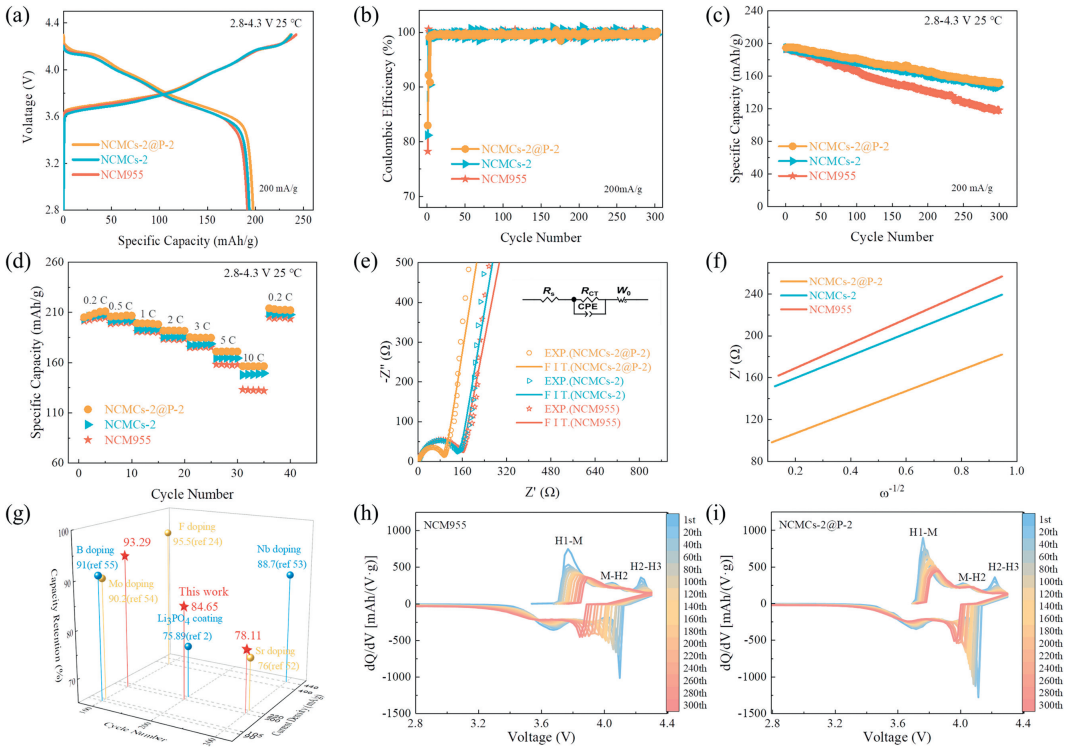

Fig. 3. (a) Initial charge–discharge curves at 1 C. (b) Coulomb efficiencies. (c) Cycle performances. (d) Rate performances. (e) EIS curves, inset as equivalent circuits. (f) The relationship between Z' and $\omega^{-1/2}$. (g) The capacity retention of NCMCs-2@P-2 cathode material after 100, 200 and 300 cycles compared with other reported nickel-rich cathode materials (Ni ≥ 0.9). Differential capacity curves of different cycles: (h) NCM955 material, (i) NCMCs-2@P-2 material.

has 16.81% higher than that of pristine NCM955 material, which fully demonstrates that the synergistic modification by Cs^+ doping and PMMA coating is very fruitful in improving the structural stability of pristine NCM955 and reducing the surface/interfacial side reactions. Among the XRD refined data in Table 1, NCMCs-2@P-2 material has the lowest Li^+/Ni^{2+} mixing degree, indicating that the low Li^+/Ni^{2+} mixing contributes to the stability of the crystal structure and thus promotes the enhancement of cyclic stability. Therefore, NCMCs-2@P-2 material achieves the most desirable cyclic stability. In order to highlight the advantages of the optimized NCMCs-2@P-2 material in this paper, Fig. 3g compares the capacity retention of NCMCs-2@P-2 material with those of other reported ultra-high nickel materials, and more details about the capacity retention at different cycles and current densities are shown in Fig. S6 and Table S1 (Supporting information) [2,23,51–54]. Obviously, the optimized NCMCs-2@P-2 material has outstanding cyclic stability, which should be attributed to the effective synergistic improvement of Cs^+ doping and PMMA coating on the internal crystal structure and surface/interface stability of NCM955 materials. Firstly, doped Cs^+ widens the layer spacing, reduces the Li^+/Ni^{2+} mixing, and improves the internal crystal structure stability. Secondly, PMMA coating can anchor Ni^{2+}, reduce the oxidative decomposition of Ni^{4+} to the electrolyte at high voltage, and effectively inhibit surface/interface side reactions, thus effectively maintaining the structural stability of the surface/interface. Fig. 3d shows the rate performances of NCM955, NCMCs-2 and NCMCs-2@P-2 materials at 0.2, 0.5, 1, 2, 3, 5 and 10 C current densities at 25 °C. It clearly indicates that the specific discharge capacity decreases with the increase of current density. The difference in the discharge specific capacity of the three materials is not large when discharged at low current density, but the difference in the discharge specific capacity becomes larger and larger after the current density is greater than 5 C, which indicates that the polarization of the materials increases dramatically during charging and discharging at high current densities and the irreversible damage to the material structure is aggravated [55]. In particular, when the current density increases to 10 C, the corresponding discharge specific capacities of the above three materials are 132.44, 148.33 and 156.36 mAh/g, respectively. In comparison, the discharge specific capacity of NCMCs-2@P-2 material has 18.06% higher than that of pristine NCM955 material. When the current density finally returned to 0.2 C, the NCMCs-2@P-2 material still has a maximum discharge specific capacity of 208.58 mAh/g. Therefore, due to the relatively stable layered crystal structure and fast Li^+ diffusion rate, NCMCs-2@P-2 material achieves the smallest polarization and the best electrochemical reversibility when discharged at high current density, and thus maintains the most desirable electrochemical performance [42,43,56].

Table 2
The R_s, R_{ct} and D_{Li^+} values of NCM955, NCMCs-2 and NCMCs-2@P-2 materials.

Samples	R_s (Ω)	R_{ct} (Ω)	D_{Li^+} (cm^2/s)
NCM955	2.743	153.4	2.003×10^{-14}
NCMCs-2	1.805	148.7	2.426×10^{-14}
NCMCs-2@P-2	1.812	95.88	2.715×10^{-14}

In order to study the electrochemical reaction kinetics of materials, electrochemical impedance spectroscopy (EIS) tests are carried out on the above three materials (Fig. 3e), and the tested batteries are not activated. The EIS plots of the three materials are typical Nyquist curves, which are generally composed of the high frequency region (Li^+ diffusion resistance through the solid electrolyte interface film and inside the active material, R_s), the middle frequency region (charge transfer resistance, R_{ct}), and the low frequency region (slope of the slash line is related to the Warburg impedance, Z_w) [32,38,42]. Table 2 is the corresponding fitting result of the equivalent circuit in Fig. 3e. It can be found that the R_s values of the three materials have little difference, but the R_{ct} val-

ues are very different. It is well known that R_{ct} value is the main factor affecting the electrochemical properties of materials. The R_{ct} value of NCMCs-2@P-2 material is only 95.88 Ω, and it is much lower than that of NCM955 (153.4 Ω) and NCMCs-2 (148.7 Ω) material, which should be attributed to the fact that Cs^+ doping reduces the Li/Ni mixing and stabilizes the interlayer structure, and PMMA coating inhibits the side reactions on the electrode surface [34,47]. The synergistic effect of the two aspects effectively accelerates the charge transfer, thus promoting the electrochemical reaction at the electrode/electrolyte interface [38,45].

The Li^+ diffusion coefficient (D_{Li^+}) is an important data to quantify the kinetics of electrochemical reactions. Therefore, we calculated D_{Li^+} by combining the fitting data of the EIS equivalent circuit and Eq. 1 [48]. In Eq. 1, R is the gas constant, T is the Kelvin temperature, n is the number of electrons transferred during the reaction, F is the Faraday constant, A is the electrode area, C is the Li^+ bulk phase concentration, and σ is the slope of the line obtained by graphing (Fig. 3f) according to Eq. 1 [48].

$$D_{Li^+} = \frac{R^2T^2}{2n^4F^4A^2C^2\sigma^2} \quad (1)$$

$$Z' = R_s + R_{ct} + \sigma \cdot \omega^{-\frac{1}{2}} \quad (2)$$

The calculated results of D_{Li^+} are shown in Table 2. It can be found that NCMCs-2@P-2 material has the largest D_{Li^+}, followed by NCMCs-2 material, and NCM955 material has the smallest D_{Li^+}, indicating that Cs^+ doping and PMMA coating can effectively improve the Li^+ diffusion rate and electrochemical reaction kinetics.

Studying the capacity attenuation mechanism of materials is helpful for us to take targeted modification measures. Figs. 3h and i show the differential capacity curve of the NCM955 and NCMCs-2@P-2 materials, which is calculated based on the charge-discharge data at different cycles. Obviously, both materials have three sets of oxidation/reduction peaks. The phase transition peak from hexagonal phase to monoclinic phase (H1 → M) appears near 3.7 V, the phase transition peak from monoclinic phase to hexagonal phase (M → H2) appears near 4.0 V, and the phase transition peak from hexagonal phase to hexagonal phase (H2 → H3) appears near 4.2 V [42,44]. In addition, it can also be found that with the increase of the cycles, the positive peak shifts towards higher voltage, and the negative peak shifts towards the opposite lower voltage, which is due to the increase of resistance and polarization [46,48,54]. Notably, the intensity attenuation of phase transition peak for NCMCs-2@P-2 material is relatively weaker than that of NCM955 material, and the voltage shift is also relatively slower. Therefore, the NCMCs-2@P-2 material has smaller polarization, more stable crystal structure, and stronger electrochemical activity at the corresponding voltage position, thus ensuring better electrochemical performance.

Galvanostatic Intermittent Titration Technique (GITT) is another important method to analyze the Li^+ diffusion coefficient of. Fig. 4a shows the GITT curves of NCM955 and NCMCs-2@P-2 materials under charging conditions. Firstly, the battery is activated for 3 cycles at 0.1 C, then charged for 10 min at 0.1 C, followed by 30 min of relaxation, and the process is repeated until the voltage reached 4.3 V. D_{Li^+} can be calculated by Eq. 3 [36].

$$D_{Li^+} = \frac{4}{\pi\tau}\left[\left(\frac{m_BV_M}{M_BS}\right)\left(\frac{\Delta E_s}{\Delta E_\tau}\right)\right]^2 \left(\tau << L^2/D\right) \quad (3)$$

where τ is the pulse duration of a single current, m_B is the mass of the active substance, V_M and M_B are the molar volume and molecular weight, respectively, S is the electrode area, ΔE_s is the voltage difference after 30 min relaxation, and ΔE_τ is the instantaneous voltage difference after a single pulse. Among them, ΔE_s and ΔE_τ can be obtained from Figs. 4c and d. Then, the calculated D_{Li^+} and voltage are plotted in Fig. 4b, it is found that the D_{Li^+} of NCMCs-2@P-2 material is higher than that of the pristine NCM955 material, indicating that Li^+ insertion/extraction is more smooth and electrochemical reaction kinetic is faster in NCMCs-2@P-2 material [39,44]. Figs. 4e and f are the relationships diagram of voltage and $\tau^{1/2}$, and they show a good linearity [37,38]. Furthermore, the single-pulse GITT curves at the beginning and end of the charging process are shown in Fig. S7 (Supporting information), and it is found that the voltage tends to be flat after 30 min of relaxation in different charging stages. Combining these two aspects, it fully shows that the GITT results calculated by us are completely reliable.

In order to have a deeper understanding of the effect of Cs^+ doping on the diffusion kinetics of Li^+ and the stability of the crystal structure, the migration energy barriers of Li^+ and Ni^{2+} are calculated by DFT theory. Figs. 4g and h are the crystal structure views of NCM955 and NCMCs-2@P-2 materials respectively, and Figs. 4i-l are the migration paths of Li^+ and Ni^{2+} of NCM955 and NCMCs-2@P-2 materials respectively. In a crystal structure, Li^+ passes from the octahedral sites along the *ab* axis to the adjacent octahedral sites *via* the tetrahedron [24,57], and Ni^{2+} migrates from the TM octahedral sites to the Li^+ octahedral sites along the *c* axis [55,58]. The theoretical calculation results show that the migration energy barrier of Li^+ in NCMCs-2@P-2 material is 0.35 eV (Fig. 4m), which is 0.26 eV lower than that of Li^+ in pristine NCM955 material. The migration energy barrier of Ni^{2+} in NCMCs-2@P-2 material is 1.52 eV (Fig. 4n), which is 0.45 eV higher than that of Ni^{2+} in pristine NCM955 material. Therefore, Cs^+ doping effectively reduces the energy barrier of Li^+ transmission and accelerates Li^+ diffusion, which is completely consistent with the results in Table 2 and Fig. 4b. At the same time, Cs^+ doping effectively increases the migration energy barrier of Ni^{2+}, which helps to suppress partial interlayer collapse caused by Li^+ insertion/extraction during the cycle [59], thus stabilizing the crystal structure of the material.

The structural stability of the surface/interface during long cycle plays an important role in the electrochemical properties of the materials. So, SEM and XPS are used to characterize the surface morphology and composition of the cathode electrode sheet after 300 cycles at 1 C (Fig. 5). Figs. 5a and b show the SEM images of NCM955 and NCMCs-2@P-2 materials after 300 cycles, respectively. It can be clearly seen that the secondary particles of NCM955 material appear serious collapse, while that of NCMCs-2@P-2 material can still maintain a relatively complete spherical structure. Figs. 5c and d are the F 1s fine XPS spectra of NCM955 and NCMCs-2@P-2 materials after 300 cycles, in which Li_xFP_y is derived from the decomposition of the electrolyte, while LiF is derived from the side reaction precipitates of the electrolyte, trace water and surface residual alkali [32,44]. In addition, the high catalytic activity of Ni^{4+} on the surface of the active substance can also catalyze the decomposition of the electrolyte, resulting in the generation of LiF and thickening of the SEI film, as well as corrosion of the cathode electrode material. As can be seen from Figs. 5c and d, the LiF content on the surface of NCMCs-2@P-2 material is 27.9%, which is much lower than 35.2% of NCM955 material, which confirms that PMMA coating can effectively reduce the side reaction between the active material and the electrolyte, and maintain the stability of the surface structure of the material. The above results can be well confirmed by the R_{ct} values in Table 2. NCMCs-2@P-2 material has a lower R_{ct} value than NCM955 material, which is due to the effective inhibition of surface/interface side reactions of NCMCs-2@P-2 material, resulting in a significant reduction of surface/interface precipitates and effective control of CEI film thickness.

Similarly, the stability of the internal crystal structure during the long cycle also plays an important role in the electrochemical properties of the material. Fig. 5e shows the cyclic performances

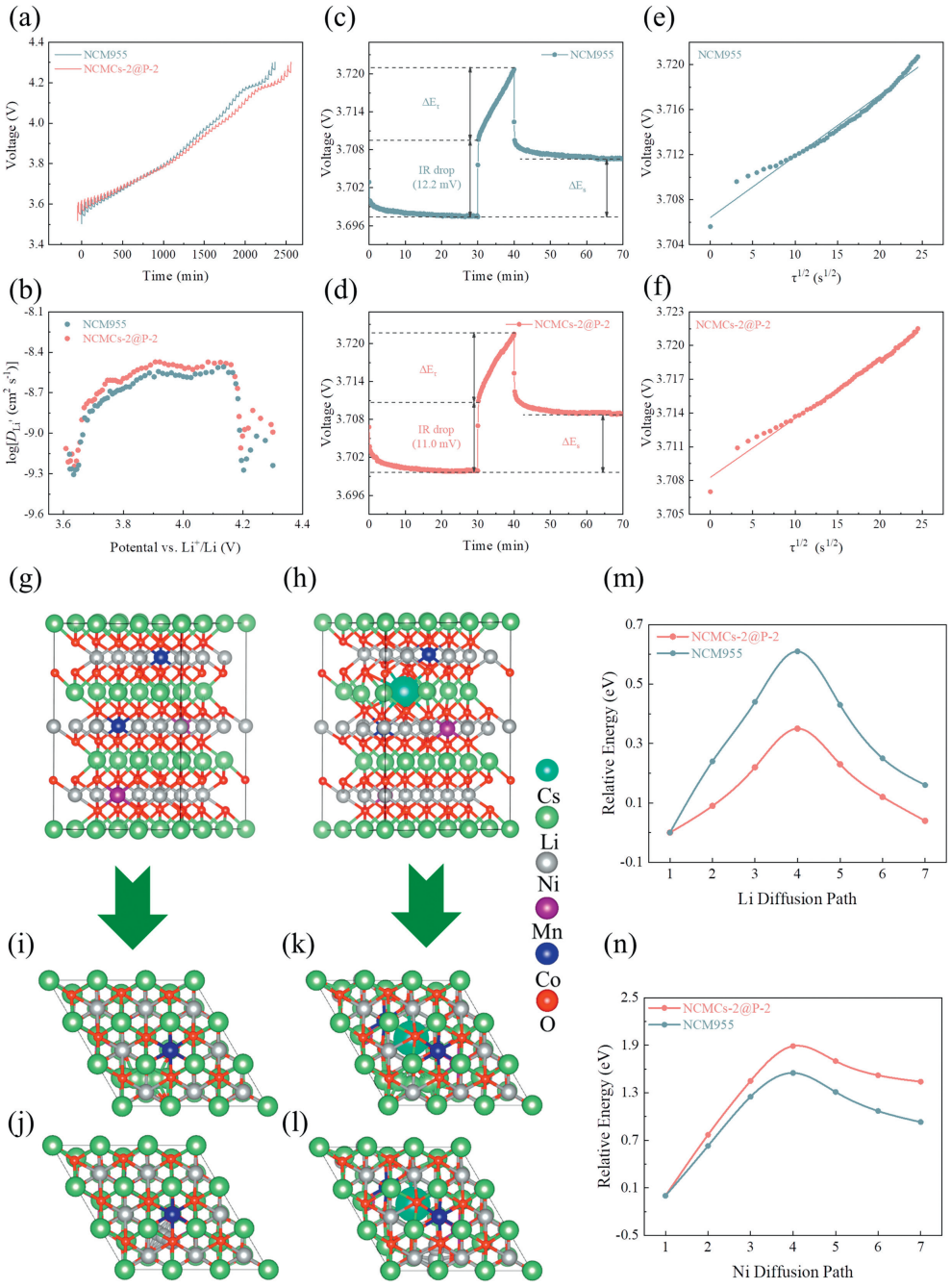

Fig. 4. (a) GITT curves in charging mode. (b) Relationship between logD_{Li+} and voltage. (c, d) Typical GITT curves of a single pulse. (e, f) Relationship between voltage and $\tau^{1/2}$. (g) Crystal structure view of NCM955 material. (h) Crystal structure view of NCMCs-2@P-2 material. (i) Li^+ migration paths in NCM955 material. (j) Ni^{2+} migration paths in NCM955 material. (k) Li^+ migration paths in NCMCs-2@P-2 material. (l) Ni^{2+} migration paths in NCMCs-2@P-2 material. (m, n) The corresponding migration energy barriers of Li^+ and Ni^{2+}.

of NCM955 and NCMCs-2@P-2 materials after 300 cycles between 2.8–4.3 V at 5 C and 25 °C. Remarkably, the Cs^+ doped and PMMA coated material has a higher discharge specific capacity (173.99 mAh/g) and a higher capacity retention rate (72.21%) at 5 C compared to the pristine NCM955 material. FIB-SEM method can be used to characterize the internal structural stability of materials after long cycles at high rates. Figs. 5f and g and Fig. S8 (Supporting information) are the cross section of NCM955 and NCMCs-2@P-2 materials achieved by FIB-SEM, respectively. Comparing the cross section cracks of the two materials, it is obvious that NCM955 material has more cracks inside, which originates from the H2 → H3 irreversible phase and leads to primary particle splitting, electrolyte penetration, and electrochemical performance degradation [42,43,60]. On the contrary, the internal structure of the secondary particles of NCMCs-2@P-2 material basically remains intact without obvious cracks between the primary particles, which indicates that the synergistic modification of Cs^+ doping and PMMA coating effectively inhibits the irreversible phase transition of H2 → H3 and the side reaction at the interface of primary particles during the long cycling process, and thus improves the stability of the internal crystal structure of the material. This will contribute to the super rate performance and cycle stability of the material. To further prove the stability of the internal crystal structure of the material after cycling, we have performed ICP tests on the elec-

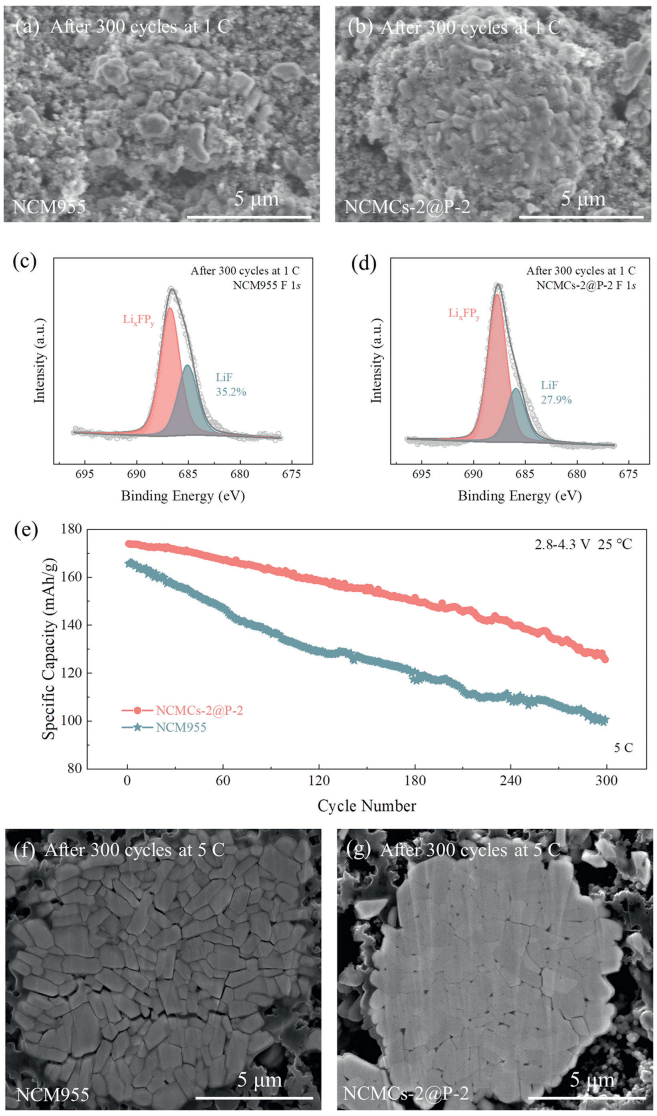

Fig. 5. SEM images of (a) NCM955 and (b) NCMCs-2@P-2 materials after 300 cycles at 1 C. F1s fine XPS spectra of (c) NCM955 and (d) NCMCs-2@P-2 materials after 300 cycles at 1 C. (e) Cycle performance of NCM955 and NCMCs-2@P-2 materials after 300 cycles at 5 C. The cross-sectional images of (f) NCM955 and (g) NCMCs-2@P-2 materials after 300 cycles at 5 C.

trolyte after cycling. Fig. S9 (Supporting information) shows that the contents of Ni, Co and Mn in the electrolyte for NCMCs-2@P-2 material are lower than those for NCM955 material, among which the reduction of Ni content is particularly obvious, indicating that the PMMA coating anchors Ni^{2+} well and effectively inhibits the side reaction between the surface/interface of NCM955 material and the electrolyte [34]. In addition, we also tested the XRD patterns of NCM955 and NCMCs-2@P-2 materials after 300 cycles at 5 C (Fig. S10 in Supporting information). It can be seen that the typical (003) peak of the pristine NCM955 material moves to a low angle, which means that its lattice expands during the cycle, causing greater stress and more obvious cracks [34].

In this paper, the structural stability, electrochemical properties and electrochemical mechanism of NCM955 material co-modified by Cs^+ doping and PMMA coating are systematically studied. A series of XRD, SEM, TEM, XPS and FIB-SEM showed that Cs^+ doping and PMMA coating can effectively reduce Li/Ni mixing, enlarge layer spacing, inhibit surface/interface side reactions, and maintain the stability of crystal structure during long cycle. DFT theoretical calculation show that NCMCs-2@P-2 material has lower Li^+ migration energy barrier and higher Ni^{2+} migration energy barrier, which is exactly consistent with the analysis of Li/Ni mixture and the calculation of Li^+ diffusion coefficient. The electrochemical test results show that NCMCs-2@P-2 material has excellent cyclic stability and rate performance. Especially in the process of high rate and long cycle, it still has a high capacity retention. Therefore, this study will provide a theoretical guidance and technical support for developing power lithium-ion battery cathode material with low cost, fast charging and long cycle life.

Declaration of competing interest

The authors declare that they have no known competing financial interests or personal relationships that could have appeared to influence the work reported in this paper.

CRediT authorship contribution statement

Hongyu Tang: Writing – original draft, Formal analysis. **Dongming Liu:** Writing – review & editing, Formal analysis. **Jinfu Huang:** Writing – review & editing. **Liang Zhang:** Writing – review & editing. **Yang Tang:** Writing – review & editing. **Bin Huang:** Writing – review & editing. **Yanwei Li:** Writing – review & editing. **Shunhua Xiao:** Writing – review & editing, Supervision, Funding acquisition. **Yiling Sun:** Writing – review & editing, Methodology, Formal analysis. **Renheng Wang:** Writing – review & editing, Methodology, Funding acquisition, Formal analysis.

Acknowledgments

This work was financially supported the National Science Foundation of China (Nos. 22362011, 22169007, 51804199), the Science and Technology Major Project of Guangxi (No. AA19046001), the Open Research Fund of Guangxi Key Laboratory of Electrochemical and Magnetochemical Functional Materials (Nos. EMFM20201105, EMFM20181119), Shenzhen Medical Research Fund (No. 20231211121324001), Shenzhen Science and Technology Program (No. KQTD20180412181422399).

Supplementary materials

Supplementary material associated with this article can be found, in the online version, at doi:10.1016/j.cclet.2024.109987.

References

[1] J.Q. Peng, Y.Y. Wei, D.M. Liu, et al., Rare Metals 43 (2023) 658–670.
[2] L. Wang, R. Wang, Q. Shi, et al., Appl. Surf. Sci. 605 (2022) 154684.
[3] Q.C. Wang, Z. Xu, X.L. Li, et al., Nano Energy 119 (2024) 109019.
[4] X. Wang, B. Zhang, Z. Xiao, et al., Chin. Chem. Lett. 34 (2023) 107772.
[5] H. Xie, H. Peng, D. Jiang, et al., Chem. Eng. J. 470 (2023) 144051.
[6] H. Jiang, X. Xu, Q. Guo, et al., J. Energy Chem. 78 (2023) 277–282.
[7] J. Liu, X. Hu, S. Qi, et al., InfoMat 6 (2024) e12507.
[8] Z. Wang, H. Zhu, H. Yu, et al., Chin. Chem. Lett. 34 (2023) 107718.
[9] L. Zhang, D. Liu, J. Huang, et al., J. Energy Storage 78 (2024) 110073.
[10] B. Hu, J. Peng, D. Liu, et al., ACS Appl. Energ. Mater. 6 (2023) 5318–5330.
[11] N. Liu, L. Chen, H. Wang, et al., Chem. Eng. J. 472 (2023) 145113.
[12] H. Hyun, H. Yoon, S. Choi, et al., Energy Environ. Sci. 16 (2023) 3968–3983.
[13] S.Q. Lu, Q. Zhang, F. Meng, et al., J. Am. Chem. Soc. 145 (2023) 7397–7407.
[14] Y.H. Luo, Q.L. Pan, H.X. Wei, et al., eScience 4 (2024) 100229.
[15] S. Liu, P.J. West, H. Zhong, et al., Chem. Mater. 35 (2023) 8857–8871.
[16] L. Ni, H. Chen, J. Gao, et al., Nano Energy 115 (2023) 108743.
[17] Y. Zhou, H. Zhang, Y. Wang, et al., ACS Nano 17 (2023) 20621–20633.
[18] G. Mao, Y. Yang, W. Jiao, et al., J. Mater. Sci. 57 (2022) 19892–19901.
[19] W. Xiao, Y. Nie, C. Miao, et al., J. Colloid Interface Sci. 607 (2022) 1071–1082.
[20] W. Zhang, X. Tang, L. Xiao, et al., J. Solid State Electrochem. 27 (2023) 1185–1194.
[21] R. Zhang, C. Wang, P. Zou, et al., Nature 610 (2022) 67–73.
[22] Z. Tan, Y. Li, X. Xi, et al., Electrochim. Acta 401 (2022) 139482.
[23] Q.Q. Qiu, S.S. Yuan, J. Bao, et al., J. Energy Chem. 61 (2021) 574–581.
[24] F. Kong, C. Liang, R.C. Longo, et al., Chem. Mater. 28 (2016) 6942–6952.
[25] W.W. Li, X.J. Zhang, J.J. Si, et al., Rare Metals 40 (2020) 1719–1726.

[26] S.T. Myung, F. Maglia, K.J. Park, et al., ACS Energy Lett. 2 (2016) 196–223.
[27] X. Xiong, D. Ding, Z. Wang, et al., J. Solid State Electrochem. 18 (2014) 2619–2624.
[28] S. Liu, H. Wu, L. Huang, et al., J. Alloys Compd. 674 (2016) 447–454.
[29] L. Ban, Y. Yin, W. Zhuang, et al., Electrochim. Acta 180 (2015) 218–226.
[30] J.H. Sung, T.W. Kim, H.K. Kang, et al., Korean J. Chem. Eng. 38 (2021) 1059–1065.
[31] B. Liu, Z. Zhang, J. Wan, et al., Ionics (Kiel) 23 (2017) 1365–1374.
[32] Y. Cao, X. Qi, K. Hu, et al., ACS Appl. Mater. Interfaces 10 (2018) 18270–18280.
[33] S.W. Doo, S. Lee, H. Kim, et al., ACS Appl. Energ. Mater. 2 (2019) 6246–6253.
[34] Y. Han, S. Heng, Y. Wang, et al., ACS Energy Lett. 5 (2020) 2421–2433.
[35] Z. Chen, G.T. Kim, Y. Guang, et al., J. Power Sources 402 (2018) 263–271.
[36] J. Leng, J. Wang, W. Peng, et al., Small 17 (2021) 2006869.
[37] H. Li, P. Zhou, F. Liu, et al., Chem. Sci. 10 (2019) 1374–1379.
[38] J. Li, X. Wang, X. Kong, et al., ACS Sustain. Chem. Eng. 9 (2021) 10547–10556.
[39] Q. Liu, X. Su, D. Lei, et al., Nat. Energy 3 (2018) 936–943.
[40] D. Hu, Y. Su, L. Chen, et al., J. Energy Chem. 58 (2021) 1–8.
[41] Y. Mao, X. Wang, S. Xia, et al., Adv. Funct. Mater. 29 (2019) 1900247.
[42] G.T. Park, H.H. Ryu, N.Y. Park, et al., J. Power Sources 442 (2019) 227242.
[43] H.H. Ryu, B. Namkoong, J.H. Kim, et al., ACS Energy Lett. 6 (2021) 2726–2734.
[44] Z. Tan, Y. Li, X. Xi, et al., ACS Sustain. Chem. Eng. 10 (2022) 3532–3545.
[45] H. Tong, Q. Zhou, B. Zhang, et al., Eng. Sci. (2020) 25–32.
[46] U.H. Kim, L.Y. Kuo, P. Kaghazchi, et al., ACS Energy Lett. 4 (2019) 576–582.
[47] Z. Ye, L. Qiu, W. Yang, et al., Chem. Eur. J. 27 (2021) 4249–4269.
[48] L. Wang, R. Wang, J. Wang, et al., ACS Appl. Mater. Interfaces 13 (2021) 8324–8336.
[49] K. Zou, M. Jiang, Z. Zhao, et al., Chem. Eng. J. 476 (2023) 146793.
[50] K. Zou, S. Xie, M. Jiang, et al., Chem. Eng. J. 483 (2024) 149189.
[51] T. Lai, A. Sheng, Z. Zhang, et al., J. Power Sources 590 (2024) 233811.
[52] X. Li, T. Lai, A. Sheng, et al., J. Energy Storage 72 (2023) 108262.
[53] G.T. Park, S.B. Kim, B. Namkoong, et al., Angew. Chem. 135 (2023) e202314480.
[54] K.J. Park, H.G. Jung, L.Y. Kuo, et al., Adv. Energy Mater. 8 (2018) 1801202.
[55] G.L. Xu, X. Liu, A. Daali, et al., Adv. Funct. Mater. 30 (2020) 2004748.
[56] L. Zhang, S. Wang, L. Zhu, et al., Nano Energy 97 (2022) 107119.
[57] H. Wu, J. Dong, Y. Zhang, et al., Adv. Funct. Mater. 33 (2023) 2303707.
[58] C. Wang, L. Han, R. Zhang, et al., Matter 4 (2021) 2013–2026.
[59] F. Wu, N. Liu, L. Chen, et al., J. Energy Chem. 62 (2021) 351–358.
[60] K Min, C. Jung, D.S. Ko, et al., ACS Appl. Mater. Interfaces 10 (2018) 20599–20610.